

# Autonomous Satellite Rendezvous and Proximity Operations with Time-Constrained Sub-Optimal Model Predictive Control

Gabriel Behrendt\* Alexander Soderlund\*\* Matthew Hale\*\*\*  
Sean Phillips\*\*\*\*

\* *University of Florida, Gainesville, FL 32611 USA (e-mail: gbehrendt@ufl.edu).*

\*\* *Space Vehicles Directorate, Air Force Research Laboratory, Kirtland AFB, NM 87108 USA (e-mail: alexander.soderlund.1@spaceforce.mil).*

\*\*\* *University of Florida, Gainesville, FL 32611 USA (e-mail: matthewhale@ufl.edu).*

\*\*\*\* *Space Vehicles Directorate, Air Force Research Laboratory, Kirtland AFB, NM 87108 USA (e-mail: sean.phillips.9@spaceforce.mil).*

---

**Abstract:** This paper presents a time-constrained model predictive control strategy for the 6 degree-of-freedom (6DOF) autonomous rendezvous and docking problem between a controllable “deputy” spacecraft and an uncontrollable “chief” spacecraft. The control strategy accounts for computational time constraints due to limited onboard processing speed. The translational dynamics model is derived from the Clohessy-Wiltshire equations and the angular dynamics are modeled on gas jet actuation about the deputy’s center of mass. Simulation results are shown to achieve the docking configuration under computational time constraints by limiting the number of allowed algorithm iterations when computing each input. Specifically, we show that upwards of 90% of computations can be eliminated from a model predictive control implementation without significantly harming control performance.

*Keywords:* Aerospace, Autonomous systems, Real-time optimal control

---

## 1. INTRODUCTION

Autonomy has become increasingly necessary for space applications due to the growing number of deployed satellites and limited ability to use human-in-the-loop control (ESA, 2022). The autonomous rendezvous and docking (ARPOD) problem is one of these applications which has gained significant interest because of recent space missions such as the NASA DART mission (Cheng et al., 2018) and its uses in applications such as satellite inspection (Bernhard et al., 2020) and servicing (Ogilvie et al., 2008). In general, the ARPOD problem requires a deputy spacecraft to maneuver to a desired state relative to a chief spacecraft.

There are a few challenges that must be addressed in the ARPOD problem to design a reliable and practically-implementable control strategy. One challenge is that the dynamics of the satellites are nonlinear when both the translational and attitude dynamics are considered together. Another challenge is that these models are subject

to disturbances such as sensor noise, model mismatch, and others unique to operations in space, such as J2 perturbations and solar pressure. Furthermore, in the design of a control strategy, we must consider that input commands must be computed using space-grade hardware. Since space-grade processors must be radiation-hardened (which requires lengthy construction cycles) to handle the electronics-hostile space environment (Bourdarie and Xapsos, 2008) and the design of space missions are often multi-year endeavors, there is a sizable processing capabilities gap between state-of-the-art, commercial off-the-shelf CPUs and their space-grade counterparts (Lovelly and George, 2017; Lovelly, 2017). A challenge of this computational gap is that space-based missions are becoming increasingly complex, particularly in the congested low-Earth orbit domain. Thus, we require a control strategy that (i) can handle nonlinearities in dynamics, (ii) is robust to perturbations, and (iii) can be computed by a computationally-limited satellite.

Often, autonomous control problems are solved via state feedback methods. Model predictive control (MPC) has been widely utilized (Falcone et al., 2007) and is a natural fit for the ARPOD problem due to its robustness and ability to handle nonlinearities. In conventional MPC, an optimization problem is solved at each time step to

---

\* Approved for public release; distribution is unlimited. Public Affairs approval #AFRL-2022-5517.

\*\*GB and MH were supported by AFOSR under grant FA9550-19-1-0169, ONR under grants N00014-19-1-2543, N00014-21-1-2495, and N00014-22-1-2435, and AFRL under grants FA8651-22-F-1052 and FA8651-08-D-0108 TO48.

completion, i.e., a new control input is computed by solving an optimization problem until a stopping condition is reached. However, given the limited available computational speed in space, we cannot reliably use conventional MPC new inputs to the system may be needed before the computations to find those inputs can be completed.

Therefore, in this work, we use a method that we refer to as *time-constrained MPC*. We consider a setting in which the underlying optimization algorithm is only allowed enough time to complete a limited number of iterations when computing each input. This constraint only allows the algorithm to make some progress toward the optimum, and, when the time constraint is reached, a sub-optimal input is applied to the system by using the optimization algorithm’s most recent iterate.

It is known in the MPC literature that the optimization problem does not need to be solved to completion in order to ensure stability of the solution (Mayne, 2014; Graichen and Käpernick, 2012; Graichen and Kugi, 2010; Pavlov et al., 2019). These works suggest that time-constrained MPC is a viable solution to account for nonlinear dynamics, perturbations, and limited onboard computational speed seen in the ARPOD problem, and this paper formalizes and confirms this point.

### 1.1 Summary of Contributions

To summarize, the contributions of this paper are:

- (1) Modeling of the ARPOD problem considering both translational and attitude dynamics
- (2) Empirical validation that time-constrained MPC succeeds in docking for the 6 DoF ARPOD problem
- (3) Empirical validation that time-constrained MPC succeeds in docking for the fully actuated 6 DoF ARPOD problem with perturbations
- (4) Comparison of performance under different computation constraints and validation that more than 90% of computations can be eliminated in the ARPOD problem without significantly harming performance

### 1.2 Related Work

The ARPOD problem has been studied in a variety of settings. Some works have considered only controlling translational (Jewison, 2017) or attitudinal dynamics (Leomanni et al., 2014; Trivailo et al., 2009). Typically, ARPOD studies consider translational control inputs that are uncoupled from the attitudinal dynamics, such as in (Hogan and Schaub, 2014). While recent studies (Soderlund et al., 2021; Soderlund and Phillips, 2022) have considered coupled translational-attitudinal systems, only two-dimensional motion between the deputy and chief was considered. Other works have developed control strategies for the more complex three-dimensional 6DOF ARPOD problem with coupled translational and attitude dynamics. These works include approaches from nonlinear control such as back-stepping (Sun and Huo, 2015; Wang and Ji, 2019), sliding mode (Yang and Stoll, 2019; Zhou et al., 2020), learning-based control (Hu et al., 2021), and artificial potential functions (Dong et al., 2018). This paper differs from those earlier works in that we do not use a

static control law with user-defined gains. Instead, we use MPC to solve for our next control input.

Model Predictive Control has been used for the 3 degree-of-freedom ARPOD problem while considering various constraints, such as collision avoidance and line-of-sight constraints (Petersen et al., 2014; Li et al., 2017; Wang et al., 2018; Richards and How, 2003; Di Cairano et al., 2012). Considering only the translational dynamics can be convenient because, under mild assumptions, the dynamics are linear. (Lee and Mesbahi, 2017) also considers a dual-quaternion formulation of the 6DOF ARPOD problem, and they use a piecewise affine approximation of the nonlinear system model so that the MPC problem can be solved quickly onboard (Hartley, 2015). Other computational considerations include using a pre-computed lookup table (Malyuta et al., 2021), or designing custom predictive controller hardware (Hartley and Maciejowski, 2013). In this paper, we differ because we consider a nonlinear dynamic model without any approximation and we explicitly address computational time constraints.

The rest of the paper is organized as follows. Section 2 presents preliminaries. Then Section 3 gives a time-constrained MPC problem statement. After that, Section 4 provides simulation results, and Section 5 concludes.

## 2. PRELIMINARIES

The Euclidean  $n$ -dimensional space is denoted by  $\mathbb{R}^n$ . The vector  $v \in \mathbb{R}^n$  is defined as  $v := (v_1, \dots, v_n)^\top$ , where the superscript  $\top$  denotes the transpose operation. Unless otherwise specified, all vectors used in this paper are *physical* vectors, meaning that they exist irrespective of any coordinate frame used. For instance, the vector  $v^{\mathcal{A}}$  denotes that the vector is given by the coordinates defined by the frame  $\mathcal{A}$ , while  $v^{\mathcal{B}}$  denotes that the vector is given by the coordinates defined by the frame  $\mathcal{B}$ . For  $v \in \mathbb{R}^3$ ,  $[v]^\times$  denotes the skew-symmetric operator, i.e.,

$$[v]^\times = \begin{bmatrix} 0 & -v_3 & v_2 \\ v_3 & 0 & -v_1 \\ -v_2 & v_1 & 0 \end{bmatrix}.$$

The  $n \times n$  identity matrix is denoted by  $I_n$ , while  $\mathbf{0}_n$  denotes the zero column vector with dimension  $n \times 1$ . Similarly, the  $n \times 1$ -dimensional column vector of ones is denoted by  $\mathbf{1}_n$ . The  $n$ -dimensional multivariate normal distribution is denoted  $\mathcal{N}(\varphi, \sigma)$ , where  $\varphi \in \mathbb{R}^n$  is the mean and  $\sigma \in \mathbb{R}^{n \times n}$  is the covariance matrix.

The Lie Group  $\mathbf{SO}(3)$  is the set of all real invertible  $3 \times 3$  matrices that are orthogonal with determinant 1, i.e.,

$$\mathbf{SO}(3) := \{R \in \mathbb{R}^{3 \times 3} \mid R^\top R = I_3, \det[R] = 1\}.$$

In this work, elements of  $\mathbf{SO}(3)$  will be referred to as *rotation matrices*. The coordinate transformation from frame  $\mathcal{B}$  to frame  $\mathcal{A}$  is given by  $v^{\mathcal{A}} = R_{\mathcal{B}}^{\mathcal{A}} v^{\mathcal{B}}$ . Any rotation matrix  $R$  can be parameterized through the unit quaternion vector  $q := \begin{pmatrix} \eta \\ \rho \end{pmatrix}$ , where  $\rho = (\rho_1, \rho_2, \rho_3)^\top \in \mathbb{R}^3$  is the vector part and  $\eta \in \mathbb{R}$  is the scalar part. The unit quaternion is contained in the unit hypersphere,  $\mathbb{S}^3$ , defined with four coordinates  $s := (s_1 \ s_2 \ s_3 \ s_4)^\top \in \mathbb{R}^4$  as  $\mathbb{S}^3 := \{s \in \mathbb{R}^4 : s^\top s = 1\}$ . The inverse quaternion is  $q^{-1} = (\eta - \rho^\top)^\top$  and the identity rotation is  $q^I = (1 \ \mathbf{0}_3^\top)^\top$ .

We use  $q_{\mathcal{B}}^{\mathcal{A}}$  to denote the quaternion corresponding to the rotation matrix  $R_{\mathcal{B}}^{\mathcal{A}}$ . The mapping from a quaternion  $q = (\eta \rho^{\top})^{\top}$  to its rotation matrix  $R$  is

$$I_3 - 2\eta[\rho]^{\times} + 2[\rho]^{\times}[\rho]^{\times}. \quad (1)$$

We note that a quaternion  $q = (\eta \rho^{\top})^{\top}$  and its negative  $-q$  represent the same physical rotation<sup>1</sup>.

This work denotes  $\omega_{\mathcal{E}\mathcal{A}}^{\mathcal{B}} \in \mathbb{R}^3$  as the angular velocity of frame  $\mathcal{A}$  relative to frame  $\mathcal{E}$  but with vector components represented in frame  $\mathcal{B}$ . The time rate change of any rotation matrix  $R_{\mathcal{B}}^{\mathcal{A}}$  is given as

$$\dot{R}_{\mathcal{B}}^{\mathcal{A}} = R_{\mathcal{B}}^{\mathcal{A}}[\omega_{\mathcal{A}\mathcal{B}}^{\mathcal{B}}]^{\times} \quad (2)$$

$$\dot{R}_{\mathcal{B}}^{\mathcal{A}} = [\omega_{\mathcal{A}\mathcal{B}}^{\mathcal{A}}]^{\times} R_{\mathcal{B}}^{\mathcal{A}}. \quad (3)$$

Analogously, the kinematics of a quaternion  $q_{\mathcal{A}}^{\mathcal{B}} = (\eta \rho^{\top})^{\top}$  are related to the angular velocity as

$$\begin{pmatrix} \dot{\eta} \\ \dot{\rho} \end{pmatrix} = -\frac{1}{2} \begin{pmatrix} -\rho^{\top} \\ \eta I_3 + [\rho]^{\times} \end{pmatrix} \omega_{\mathcal{A}\mathcal{B}}^{\mathcal{A}}. \quad (4)$$

### 3. PROBLEM STATEMENT

#### 3.1 Conventional Model Predictive Control

In this section, we introduce conventional MPC, then explain how time-constrained MPC differs from it. Consider the discrete-time dynamics  $x(k+1) = f_d(x(k), u(k))$ , where  $x(k) \in \chi \subset \mathbb{R}^n$ ,  $u(k) \in \mathcal{U} \subset \mathbb{R}^m$ , and  $f_d : \chi \times \mathcal{U} \rightarrow \chi$ . The goal of conventional MPC is to solve an optimal control problem at each timestep  $k$  over a finite prediction horizon of length  $N \in \mathbb{N}$ , using the current state as the initial state. This process generates the control sequence  $\mathbf{u}^*(k) = \{u^*(k), u^*(k+1), \dots, u^*(N-1)\}$  and the state sequence  $\mathbf{x}^*(k) = \{x^*(k), x^*(k+1), \dots, x^*(N)\}$ .

Then, the first input in this sequence,  $u^*(k)$ , is applied to the system and this process is repeated until the end of the time horizon is reached. Formally, the conventional MPC problem that is solved at each time  $k$  is given next.

*Problem 1. (Conventional MPC).*

$$\underset{\mathbf{u}(k)}{\text{minimize}} J(x(k), \mathbf{u}(k)) = \sum_{i=k}^{N-1} \ell(x(i), u(i))$$

subject to  $x(k) = x(0)$

$$x(N) \in \chi_f$$

$$x(i+1) = f_d(x(i), u(i)), \quad i = k, k+1, \dots, N-1$$

$$u_{\min} \leq u(i) \leq u_{\max}, \quad i = k, k+1, \dots, N-1$$

$$\mathbf{u}(k) \in \mathcal{U}_N,$$

where  $\ell : \chi \times \mathcal{U} \rightarrow \mathbb{R}$  is the cost functional,  $\chi_f \subseteq \chi$  is the terminal constraint set,  $u_{\min}, u_{\max} \in \mathcal{U}$  are input limits,  $\mathbf{u}(k) = \{u(k), \dots, u(N-1)\}$ , and  $\mathcal{U}_N$  is the set of admissible inputs<sup>2</sup>.

#### 3.2 Time-Constrained MPC

In conventional MPC, Problem 1 is iteratively solved to completion at each time  $k$  by reaching a stopping condition

<sup>1</sup> This work has opted to adopt the convention of (Kuipers, 1999) where the passive rotation operator on a vector  $v$  is represented as  $q^{-1} \otimes v \otimes q$  where  $v$  is a ‘‘pure’’ quaternion with 0 scalar part. This choice affects the signs of Eq.(1) and the angular velocity kinematics.

<sup>2</sup> We refer the reader to (Grüne and Pannek, 2017, Definition 3.9) for a formal definition of an admissible control sequence.

based on the optimality of the solution. We use  $j_k$  to denote the number of iterations that an optimization algorithm must complete to reach a stopping condition in the computation of  $\mathbf{u}(k)$ . In computationally constrained settings, it cannot be guaranteed that there is time to execute all  $j_k$  desired iterations because a system input may be needed before those computations are completed. Therefore, we employ the following time-constrained MPC problem that has an explicit constraint on  $j_k$ .

*Problem 2. (Time-Constrained MPC).*

$$\underset{\mathbf{u}(k)}{\text{minimize}} J(x(k), \mathbf{u}(k)) = \sum_{i=k}^{N-1} \ell(x(i), u(i))$$

subject to  $x(k) = x(0)$

$$x(N) \in \chi_f$$

$$x(i+1) = f_d(x(i), u(i)), \quad i = k, k+1, \dots, N-1$$

$$u_{\min} \leq u(i) \leq u_{\max}, \quad i = k, k+1, \dots, N-1$$

$$\mathbf{u}(k) \in \mathcal{U}_N$$

$$j_k \leq j_{\max},$$

where  $j_k$  is the number of iterations computed at time  $k$  and  $j_{\max}$  is the maximum allowable iterations for all  $k$ .

The constraint  $j_k \leq j_{\max}$  models scenarios with limited onboard computational speed in which there is only enough time to complete at most  $j_{\max}$  iterations. A solution to Problem 2 at time  $k$  will typically result in a sub-optimal input and state sequences, i.e.,

$$\tilde{\mathbf{u}}(k) = \{\tilde{u}(k), \tilde{u}(k+1), \dots, \tilde{u}(N-1)\}$$

$$\tilde{\mathbf{x}}(k) = \{\tilde{x}(k), \tilde{x}(k+1), \dots, \tilde{x}(N)\},$$

respectively. Then, we apply the first input of the resulting input sequence, namely  $\tilde{u}(k)$ , and repeat this process until the end of the time horizon is reached. This setup is different from conventional MPC in that we apply a potentially sub-optimal input due to the iteration constraint  $j_k \leq j_{\max}$  in Problem 2. Next, we derive the dynamics for the 6DOF ARPOD problem that will be used in our setup and solution to Problem 2.

#### 3.3 Dynamics Overview

The objective of this work is to design an autonomous controller such that a deputy spacecraft’s translational and attitudinal states converge to a successful docking configuration with the chief, as shown in Figure 1. Three frames of reference are used:

- (1) The Earth-Centered Inertial (ECI) frame originating from the Earth’s center is denoted  $\mathcal{E} := \{\hat{\mathbf{x}}_{\mathbf{e}}, \hat{\mathbf{y}}_{\mathbf{e}}, \hat{\mathbf{z}}_{\mathbf{e}}\}$ .
- (2) The Clohessy-Wiltshire (CW) frame is a non-inertial frame attached to the chief satellite, denoted  $\mathcal{O} := \{\hat{\mathbf{x}}_{\mathbf{o}}, \hat{\mathbf{y}}_{\mathbf{o}}, \hat{\mathbf{z}}_{\mathbf{o}}\}$ . The origin lies at the center of mass of the chief, unless otherwise specified. The  $\hat{\mathbf{x}}_{\mathbf{o}}$ -axis aligns with the vector pointing from the center of the Earth towards the center of mass of the chief satellite. The  $\hat{\mathbf{z}}_{\mathbf{o}}$ -axis is in the direction of the orbital angular momentum vector of the chief spacecraft. The  $\hat{\mathbf{y}}_{\mathbf{o}}$ -axis completes the right-handed orthogonal frame.
- (3) The deputy-fixed frame is a non-inertial body-fixed frame attached to the deputy satellite and denoted  $\mathcal{D} := \{\hat{\mathbf{x}}_{\mathbf{d}}, \hat{\mathbf{y}}_{\mathbf{d}}, \hat{\mathbf{z}}_{\mathbf{d}}\}$ . The origin is assumed to lie at the center of mass of the deputy, unless otherwise specified. We use the convention that the  $\hat{\mathbf{x}}_{\mathbf{d}}$ -axis

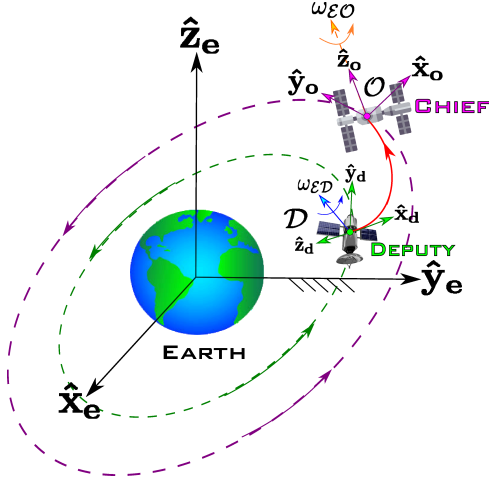


Fig. 1. The chief (with rotating orbit-fixed frame  $\mathcal{O}$ ) and a deputy (with body-fixed frame  $\mathcal{D}$ ) are orbiting about the Earth with inertial frame  $\mathcal{E}$ . The dashed lines are the closed orbital trajectories of both spacecraft. The red solid line depicts the rendezvous trajectory from the deputy to the chief as seen in the inertial frame.

is along the starboard direction,  $\hat{y}_d$  is in the fore direction, and  $\hat{z}_d$  completes the right-handed frame in the topside direction.

Let  $(m_c, J^c)$  and  $(m_d, J^d)$  be the mass-inertia pairs of the chief and deputy respectively. We make the following assumptions regarding their relative motion dynamics:

*Assumption 1.* Both the chief and the deputy spacecraft are assumed to be rigid bodies of constant mass

*Assumption 2.* The chief-fixed frame is assumed to always align with the orbit-fixed frame  $\mathcal{O}$ .

*Assumption 3.* The chief spacecraft is in an uncontrolled, circular orbit.

*Assumption 4.* The distance between the chief and the deputy is much less than the distance between the Earth and the chief.

*Assumption 5.* The deputy spacecraft has bi-directional thrusters and external torque-generators installed along the axes aligning with its body-fixed frame.

*Assumption 6.* The axes of the deputy-fixed frame are aligned with the principal axes of the deputy body.

The position and velocity of the deputy relative to the chief with respect to the CW frame  $\mathcal{O}$  are

$$\delta r^{\mathcal{O}} := (\delta x \ \delta y \ \delta z)^\top \text{ and } \delta \dot{r}^{\mathcal{O}} := (\delta \dot{x} \ \delta \dot{y} \ \delta \dot{z})^\top.$$

Assumptions A3-A5 allow the use of the Clohessy-Wiltshire translational dynamics (see (Curtis, 2013)) with deputy controls, expressed as

$$\begin{pmatrix} \delta \dot{x} \\ \delta \dot{y} \\ \delta \dot{z} \\ \delta \ddot{x} \\ \delta \ddot{y} \\ \delta \ddot{z} \end{pmatrix} = \begin{pmatrix} 0 & 0 & 0 & 1 & 0 & 0 \\ 0 & 0 & 0 & 0 & 1 & 0 \\ 0 & 0 & 0 & 0 & 0 & 1 \\ 3n^2 & 0 & 0 & 0 & 2n & 0 \\ 0 & 0 & 0 & -2n & 0 & 0 \\ 0 & 0 & -n^2 & 0 & 0 & 0 \end{pmatrix} \begin{pmatrix} \delta x \\ \delta y \\ \delta z \\ \delta \dot{x} \\ \delta \dot{y} \\ \delta \dot{z} \end{pmatrix} + \begin{pmatrix} \mathbf{0}_{3 \times 3} \\ \frac{1}{m_d} R_{\mathcal{O}}^{\mathcal{D}} \end{pmatrix} F_d^{\mathcal{D}}, \quad (5)$$

where the ‘‘mean motion’’ constant is  $n = \sqrt{\frac{\mu}{|r_c|^3}}$  in  $\text{rad} \cdot \text{s}^{-1}$ ,  $\mu = 398600.4418 \text{ km}^3 \text{ s}^{-2}$  is the Earth’s standard gravitational parameter and  $r_c$  is the radius of the chief’s circular orbit.

### 3.4 Attitude Dynamics - Chief Frame

Note the rotation  $R_{\mathcal{D}}^{\mathcal{O}}$  applied to the deputy thrust vector  $F_d^{\mathcal{D}}$  in (5). Both frames  $\mathcal{O}$  and  $\mathcal{D}$  are rotating with respect to the inertial frame  $\mathcal{E}$ . The angular velocity equations are  $\omega_{\mathcal{E}\mathcal{D}}^{\mathcal{O}} := (\omega_1 \ \omega_2 \ \omega_3)^\top$ ,  $\omega_{\mathcal{O}\mathcal{D}}^{\mathcal{O}} := (\delta\omega_1 \ \delta\omega_2 \ \delta\omega_3)^\top$ , and  $\omega_{\mathcal{E}\mathcal{O}}^{\mathcal{O}} := (0 \ 0 \ n)^\top$ . The deputy external torque vector in the  $\mathcal{O}$  frame is  $\tau^{\mathcal{O}} := (\tau_1 \ \tau_2 \ \tau_3)^\top$  and from assumption A6 the deputy inertia matrix in the deputy-fixed frame is

$$J^{\mathcal{D}} = \begin{pmatrix} J_1 & 0 & 0 \\ 0 & J_2 & 0 \\ 0 & 0 & J_3 \end{pmatrix}.$$

The angular velocity of the  $\mathcal{D}$  frame relative to the  $\mathcal{O}$  frame is  $\omega_{\mathcal{O}\mathcal{D}}^{\mathcal{E}} = \omega_{\mathcal{E}\mathcal{D}}^{\mathcal{E}} - \omega_{\mathcal{E}\mathcal{O}}^{\mathcal{E}}$ , with the time derivatives given by

$$\dot{\omega}_{\mathcal{O}\mathcal{D}}^{\mathcal{E}} = \dot{\omega}_{\mathcal{E}\mathcal{D}}^{\mathcal{E}} - \dot{\omega}_{\mathcal{E}\mathcal{O}}^{\mathcal{E}}. \quad (6)$$

From (2) and (3) we yield the relations

$$\begin{aligned} \dot{\omega}_{\mathcal{O}\mathcal{D}}^{\mathcal{E}} &= R_{\mathcal{O}}^{\mathcal{E}} [\omega_{\mathcal{E}\mathcal{O}}^{\mathcal{O}}]^\times \omega_{\mathcal{O}\mathcal{D}}^{\mathcal{O}} + R_{\mathcal{O}}^{\mathcal{E}} \dot{\omega}_{\mathcal{O}\mathcal{D}}^{\mathcal{O}} \\ \dot{\omega}_{\mathcal{E}\mathcal{O}}^{\mathcal{E}} &= R_{\mathcal{O}}^{\mathcal{E}} \underbrace{[\omega_{\mathcal{E}\mathcal{O}}^{\mathcal{O}}]^\times \omega_{\mathcal{E}\mathcal{O}}^{\mathcal{O}}}_{=0} + R_{\mathcal{O}}^{\mathcal{E}} \underbrace{\dot{\omega}_{\mathcal{E}\mathcal{O}}^{\mathcal{O}}}_{=0} = 0 \\ \dot{\omega}_{\mathcal{E}\mathcal{D}}^{\mathcal{E}} &= R_{\mathcal{D}}^{\mathcal{E}} \underbrace{[\omega_{\mathcal{E}\mathcal{D}}^{\mathcal{D}}]^\times \omega_{\mathcal{E}\mathcal{D}}^{\mathcal{D}}}_{=0} + R_{\mathcal{D}}^{\mathcal{E}} \dot{\omega}_{\mathcal{E}\mathcal{D}}^{\mathcal{D}}. \end{aligned}$$

Substituting these into a manipulation of (6) gives the relation  $\dot{\omega}_{\mathcal{O}\mathcal{D}}^{\mathcal{O}} = R_{\mathcal{D}}^{\mathcal{O}} \dot{\omega}_{\mathcal{E}\mathcal{D}}^{\mathcal{D}} - [\omega_{\mathcal{E}\mathcal{O}}^{\mathcal{O}}]^\times \omega_{\mathcal{O}\mathcal{D}}^{\mathcal{O}}$ . Let the deputy body have inertia matrix  $J^{\mathcal{D}}$  as measured in the deputy-fixed frame with external control torque vector  $\tau^{\mathcal{D}}$  being applied about the center of mass. From Euler’s second law of motion we have

$$\dot{\omega}_{\mathcal{E}\mathcal{D}}^{\mathcal{D}} = -K^{\mathcal{D}} [\omega_{\mathcal{E}\mathcal{D}}^{\mathcal{D}}]^\times [J^{\mathcal{D}} \omega_{\mathcal{E}\mathcal{D}}^{\mathcal{D}}] + K^{\mathcal{D}} \tau^{\mathcal{D}}, \quad (7)$$

where  $K^{\mathcal{D}} := [J^{\mathcal{D}}]^{-1}$ . Application of rotational transformation to (7) gives

$$\dot{\omega}_{\mathcal{O}\mathcal{D}}^{\mathcal{O}} = R_{\mathcal{D}}^{\mathcal{O}} [-K^{\mathcal{D}} [\omega_{\mathcal{E}\mathcal{D}}^{\mathcal{D}}]^\times [J^{\mathcal{D}} \omega_{\mathcal{E}\mathcal{D}}^{\mathcal{D}}] + K^{\mathcal{D}} \tau^{\mathcal{D}}] - [\omega_{\mathcal{E}\mathcal{O}}^{\mathcal{O}}]^\times \omega_{\mathcal{O}\mathcal{D}}^{\mathcal{O}},$$

which expands to

$$\begin{aligned} \dot{\omega}_{\mathcal{O}\mathcal{D}}^{\mathcal{O}} &= [\omega_{\mathcal{O}\mathcal{D}}^{\mathcal{O}}]^\times \omega_{\mathcal{E}\mathcal{O}}^{\mathcal{O}} + K^{\mathcal{O}}(t) \tau^{\mathcal{O}} \\ &\quad - K^{\mathcal{O}}(t) ([\omega_{\mathcal{O}\mathcal{D}}^{\mathcal{O}}]^\times [J^{\mathcal{D}} R_{\mathcal{O}}^{\mathcal{D}} \omega_{\mathcal{O}\mathcal{D}}^{\mathcal{O}}] + [\omega_{\mathcal{O}\mathcal{D}}^{\mathcal{O}}]^\times [J^{\mathcal{D}} R_{\mathcal{O}}^{\mathcal{D}} \omega_{\mathcal{E}\mathcal{O}}^{\mathcal{O}}] \\ &\quad + [\omega_{\mathcal{E}\mathcal{O}}^{\mathcal{O}}]^\times [J^{\mathcal{D}} R_{\mathcal{O}}^{\mathcal{D}} \omega_{\mathcal{O}\mathcal{D}}^{\mathcal{O}}] + [\omega_{\mathcal{E}\mathcal{O}}^{\mathcal{O}}]^\times [J^{\mathcal{D}} R_{\mathcal{O}}^{\mathcal{D}} \omega_{\mathcal{E}\mathcal{O}}^{\mathcal{O}}]). \end{aligned} \quad (8)$$

Here  $K^{\mathcal{O}} = R_{\mathcal{D}}^{\mathcal{O}} K^{\mathcal{D}} R_{\mathcal{O}}^{\mathcal{D}}$  is a time-varying inertia matrix.

### 3.5 Docking Configuration

To achieve a successful docking configuration, the deputy must reach a set of predefined relative translational and attitudinal states. Let  $\tilde{q}_{\mathcal{D}}^{\mathcal{O}}$  be the quaternion representing the desired rotation from the deputy  $\mathcal{D}$  frame to the CW  $\mathcal{O}$  frame, and let  $q_{\mathcal{D}}^{\mathcal{O}}$  be the actual (i.e., plant-state) rotation quaternion. Analogously, let  $\tilde{\omega}_{\mathcal{O}\mathcal{D}}^{\mathcal{O}}$  be the desired relative angular velocity and  $\omega_{\mathcal{O}\mathcal{D}}^{\mathcal{O}}$  be the actual relative angular velocity. Lastly, let  $\delta q_{\mathcal{D}}^{\mathcal{O}} := \{\tilde{q}_{\mathcal{D}}^{\mathcal{O}}\}^{-1} \otimes q_{\mathcal{D}}^{\mathcal{O}}$  and  $\delta \omega_{\mathcal{O}\mathcal{D}}^{\mathcal{O}} := \omega_{\mathcal{O}\mathcal{D}}^{\mathcal{O}} - \tilde{\omega}_{\mathcal{O}\mathcal{D}}^{\mathcal{O}}$  respectively denote the error quaternion and error angular velocity.

To achieve on-orbit attitudinal synchronization between both spacecraft, the aim is to drive  $\delta q_{\mathcal{D}}^{\mathcal{O}} \rightarrow q^I$  and  $\delta \omega_{\mathcal{O}\mathcal{D}}^{\mathcal{O}} \rightarrow \mathbf{0}_3$ . In the ARPOD problem,  $\tilde{q}_{\mathcal{D}}^{\mathcal{O}} = q^I$  and  $\tilde{\omega}_{\mathcal{O}\mathcal{D}}^{\mathcal{O}} = \mathbf{0}_3$ , which results in the attitudinal error kinematics  $\delta \dot{q}_{\mathcal{D}}^{\mathcal{O}} =$

$\frac{1}{2}[\delta\rho_{\mathcal{D}}^{\mathcal{O}}]^{\top}\delta\omega_{\mathcal{O}\mathcal{D}}^{\mathcal{O}}$  and  $\delta\rho_{\mathcal{D}}^{\mathcal{O}} = -\frac{1}{2}[\delta\eta_{\mathcal{D}}^{\mathcal{O}}I_3 + [\delta\rho_{\mathcal{D}}^{\mathcal{O}}]^{\times}]\delta\omega_{\mathcal{O}\mathcal{D}}^{\mathcal{O}}$ . Relative translational states required for docking are  $\delta r^{\mathcal{O}} = \mathbf{0}_3$  and  $\delta\dot{r}^{\mathcal{O}} = \mathbf{0}_3$ . The state vector of interest is

$$x := \left([\delta r^{\mathcal{O}}]^{\top}, [\delta\dot{r}^{\mathcal{O}}]^{\top}, \delta\eta_{\mathcal{D}}^{\mathcal{O}}, [\delta\rho_{\mathcal{D}}^{\mathcal{O}}]^{\top}, [\delta\omega_{\mathcal{O}\mathcal{D}}^{\mathcal{O}}]^{\top}\right)^{\top} \in \chi$$

and the objective docking state be

$$x_d := ([\mathbf{0}_3]^{\top}, [\mathbf{0}_3]^{\top}, 1, [\mathbf{0}_3]^{\top}, [\mathbf{0}_3]^{\top})^{\top} \in \chi.$$

This vector  $x_d$  indicates that the frame  $\mathcal{O}$  has the same origin, linear velocity, orientation, and angular velocity as frame  $\mathcal{D}$ . Let the control vector of interest in frame  $\mathcal{O}$  be  $u := ([F_d^{\mathcal{D}}]^{\top}, [\tau^{\mathcal{D}}]^{\top})^{\top} \in \mathcal{U}$  and the objective inputs be  $u_d := ([\mathbf{0}_3]^{\top}, [\mathbf{0}_3]^{\top})^{\top} \in \mathcal{U}$ . Let us define  $z(k) := [u(k)^{\top} x(k)^{\top}]^{\top}$  and  $z_d := [u_d^{\top} x_d^{\top}]^{\top}$ . The next section uses this model to solve the ARPOD problem using time-constrained MPC.

## 4. MAIN RESULTS

In this section we present two simulations. First, we consider time-constrained MPC with unperturbed states. Second, we consider states affected by perturbations to illustrate the robustness of time-constrained MPC.

### 4.1 Time-Constrained MPC for ARPOD

The problem we solve in this section is given next.

*Problem 3.* (Time-Constrained MPC for ARPOD).

$$\underset{\mathbf{u}(k)}{\text{minimize}} J(x(k), \mathbf{u}(k)) =$$

$$\sum_{i=k}^{N-1} (x(i) - x_d)^{\top} Q (x(i) - x_d) + u(i)^{\top} R u(i)$$

subject to  $x(k) = x(0)$

$$x(N) = x_d$$

$$x(i+1) = g_d(x(i), u(i)), \quad i = k, k+1, \dots, N-1$$

$$u_{\min} \leq u(i) \leq u_{\max}, \quad i = k, k+1, \dots, N-1$$

$$\mathbf{u}(k) \in \mathcal{U}_N$$

$$j_k \leq j_{\max},$$

where  $Q \in \mathbb{R}^{13 \times 13}$ ,  $R \in \mathbb{R}^{6 \times 6}$ ,  $u_{\min} := (-10^{-3} \times \mathbf{1}_3^{\top}, -10^{-4} \times \mathbf{1}_3^{\top})^{\top}$ ,  $u_{\max} := -u_{\min}$ , and  $g_d : \chi \times \mathcal{U} \rightarrow \chi$  are the discretized versions of (4), (5), and (8) generated by the fourth-order Runge-Kutta method.

### 4.2 Unperturbed Results

We consider the problem parameters and initial states in Table 1, where  $n$  is the chief mean motion,  $m_d$  is the mass of the deputy, and  $J_d$  is its moment of inertia matrix. The values in Table 1 represent a chief spacecraft in low Earth orbit and a deputy in a typical ARPOD initial condition.

The cost matrices used were  $Q = \text{diag}([10 \times \mathbf{1}_3^{\top}, 10^{-4} \times \mathbf{1}_3^{\top}, 10^8 \times \mathbf{1}_7^{\top}])$  and  $R = \text{diag}([10^3 \times \mathbf{1}_3^{\top}, 10^{10} \times \mathbf{1}_3^{\top}])$ . We considered the prediction horizon  $N = 1000$  and sampling time  $t_s = 3s$ . Since the torque inputs and attitudinal states are heavily penalized, the orientation of the deputy is prioritized over the translational state. We formulated Problem 3 in MATLAB using the CasADi symbolic framework and solved it using Ipopt (Wächter and Biegler, 2006).

In the minimization of Problem 3, at each time  $k$  we designed two stopping conditions, either of which terminates

Table 1: Problem Parameters and Initial State

Parameter	Value	Units
$n$	-0.0011	rad/s
$m_d$	12	kg
$J_d$	$\text{diag}([0.2734, 0.2734, 0.3125])$	$\text{kg}\cdot\text{m}^2$
$\omega_{\mathcal{E}\mathcal{O}}^{\mathcal{O}}$	$(0 \ 0 \ -0.0011)^{\top}$	rad/s
$\delta r^{\mathcal{O}}$	$(1.5 \ -1.77 \ 3)^{\top}$	km
$\delta\dot{r}^{\mathcal{O}}$	$(0.001 \ 0.0034 \ 0)^{\top}$	km/s
$q_{\mathcal{D}}^{\mathcal{O}}$	$(0.7715 \ 0.4629 \ 0.3086 \ 0.3086)^{\top}$	
$\omega_{\mathcal{O}\mathcal{D}}^{\mathcal{O}}$	$(0 \ 0 \ -0.005)^{\top}$	rad/s

Table 2: Solver times and reductions for Problem 3 without perturbations

$j_{\max}$	Average Time/Loop Reduction (s)	Average Time/Loop Reduction (%)	Maximum Loop Time Reduction (s)	Maximum Loop Time Reduction (%)
2	0.5159	30.52%	26.40	95.59%
3	0.4245	25.11%	26.09	94.48%
4	0.4283	25.33%	25.75	93.26%
5	0.4054	23.98%	25.43	92.09%

the minimization if it is met: (1) the change in objective function value at consecutive iterations was less than a specified tolerance or (2) the algorithm had completed the maximum allowable number of iterations, i.e.,  $j_k = j_{\max}$ , to enforce the computational time constraint. In this subsection, we declare that we have achieved the docking configuration when  $\|z(k) - z_d\|_{\infty} \leq 10^{-3}$ .

Figure 2 shows the distance between the current state  $x(k)$  and docking configuration  $x_d$  over time for multiple values of  $j_{\max}$ . The error  $\|x(k) - x_d\|_2$  decreases faster as we allow more iterations to occur, which agrees with the intuition that more computations drive an algorithm's iterates closer to an optimum. We can observe that the optimal trajectory, i.e., the one computed with  $j_{\max} = \infty$ , achieves the docking state in the shortest amount of time.

Furthermore, there is a trade-off between the value of  $j_{\max}$  and time it takes to reach  $x_d$ . This is shown in Figure 3, where we plot the absolute difference between the time-constrained and optimal error. In addition, Figures 4 and 5 show that the attitudinal and translational states achieve the docking configuration given the initial conditions in Table 1 with  $j_{\max} = 3$ . Figure 6 shows the positional trajectories in 3-D space achieving the docking configuration. A Monte Carlo simulation was performed with  $j_{\max} = 3$  and the average error for 50 initial conditions was  $2.6 \cdot 10^{-3}$ . These results show that time-constrained MPC can control the deputy to the docking configuration using unperturbed states. Table 2 shows that we achieve at least a 23.98% reduction in average time to solve Problem 3 at each time  $k$ , for all values of  $j_{\max}$  that we used. Moreover, Table 2 shows a reduction of more than 92% in the maximum loop time for the worst case solving time for all  $j_{\max}$ . Next, we demonstrate the robustness of time-constrained MPC to perturbations.

### 4.3 Perturbed Results

One advantage of MPC is robustness to perturbations. In these simulations, at each time  $k$ , we add a disturbance  $\omega(k)$  to the state  $x(k)$ . The initial state for the next MPC loop, at time  $k+1$  was  $x(0) = g_d(x(k), u(k)) + \omega(k)$ . The components of the perturbation vector  $\omega(k) \in \mathbb{R}^{13}$  were sampled from multivariate normal distributions as

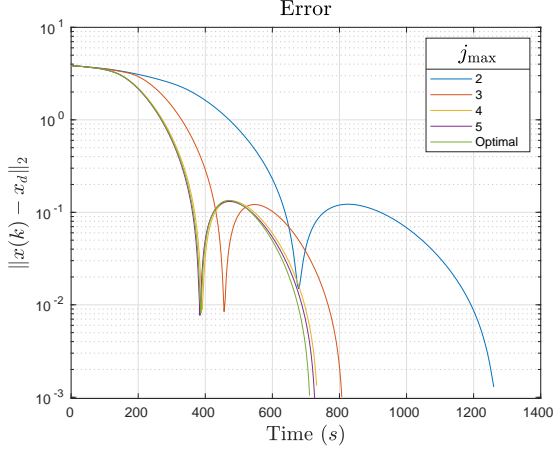


Fig. 2. Plot of the unperturbed error  $\|x(k) - x_d\|_2$  as a function of time for various values of  $j_{max}$ .

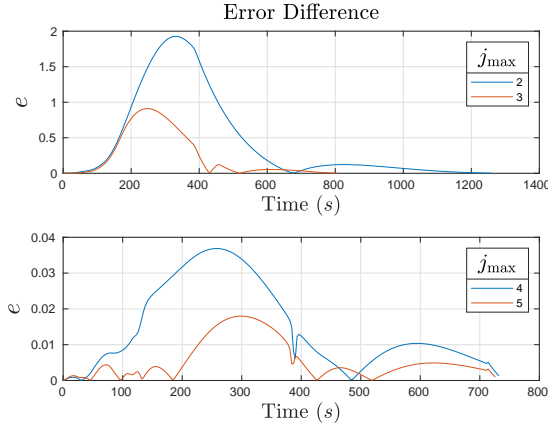


Fig. 3. Comparison plot of the difference between time-constrained and optimal unperturbed error as a function of time. The value of  $e := \|\tilde{x}(k) - x_d\|_2 - \|x^*(k) - x_d\|_2$  is shown for various values of  $j_{max}$ .

$$\omega(k) \sim \begin{pmatrix} 10^{-3} \times \mathcal{N}(\mathbf{0}_3, I_3) \\ 10^{-6} \times \mathcal{N}(\mathbf{0}_3, I_3) \\ 10^{-8} \times \mathcal{N}(\mathbf{0}_4, I_4) \\ 10^{-6} \times \mathcal{N}(\mathbf{0}_3, I_3) \end{pmatrix}.$$

We consider the same initial condition from Table 1 and same problem parameters from the previous subsection. In this subsection, we declare that we have achieved the docking configuration when  $\|z(k) - z_d\|_\infty \leq 5 \times 10^{-3}$ . Figure 7 shows that the deputy still achieves the docking configuration with the chief subject to perturbations and limited computational time. It takes more time to achieve the docking configuration for each  $j_{max}$  compared to the unperturbed case (cf. Figure 2).

The optimal error trajectory takes longer to reach zero than the error trajectories generated under the computational time constraint. This differs from the unperturbed case and is perhaps counterintuitive, but is easily explained. The optimal error trajectory takes longer to reach zero because the control inputs are computed using our dynamic model without knowledge of the perturbations. Because future perturbations are unknown, exactly solving for an optimum while predicting future states does not

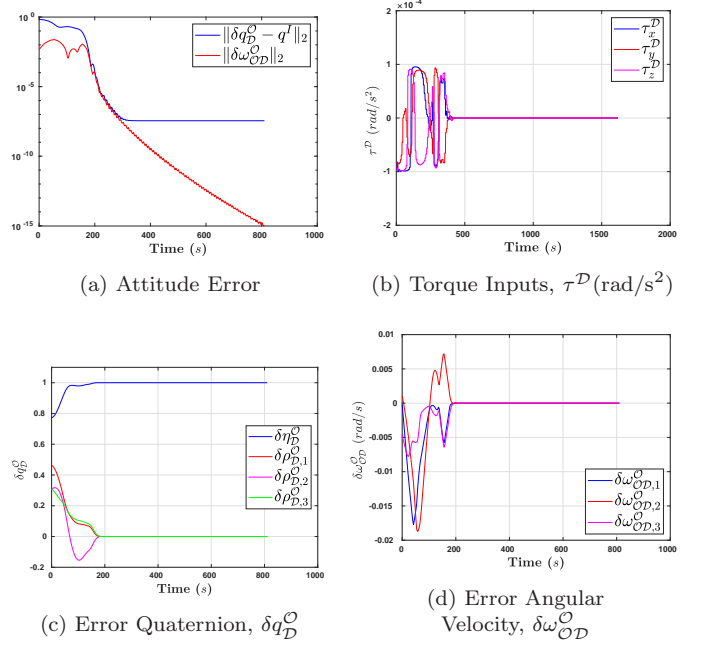


Fig. 4. Plots of the unperturbed attitudinal error, states, and torque inputs for  $j_{max} = 3$ .

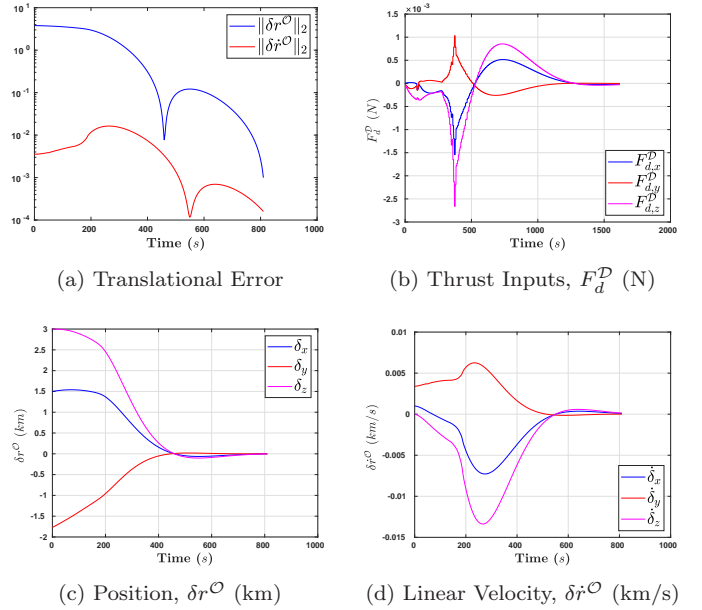


Fig. 5. Plots of the unperturbed translational error, states, and thrust inputs for  $j_{max} = 3$ .

necessarily give the best performance. In Figures 8 and 9 we show the states and inputs under perturbations for the initial conditions in Table 1 and  $j_{max} = 3$ .

These plots are similar to the unperturbed case but we can see the effect of perturbations, especially in the attitude error in Figure 8a. In all cases, the docking configuration is successfully reached. Table 3 shows that we achieve at least a 23.98% reduction in average solving time per MPC loop for all values of  $j_{max}$ . Table 3 also shows a roughly 95% reduction in the worst case solving time for all  $j_{max}$ .

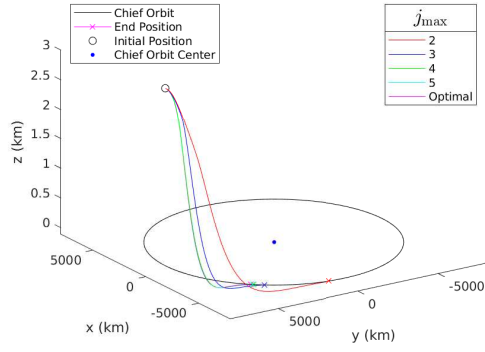


Fig. 6. Plot of the the position of the deputy docking with the target is shown for the unperturbed case for various values of  $j_{max}$ .

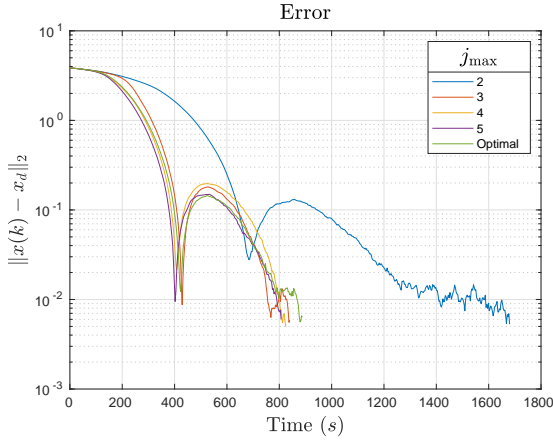


Fig. 7. Plot of the perturbed error,  $\|x(k) - x_d\|_2$ , as a function of time for various values of  $j_{max}$ .

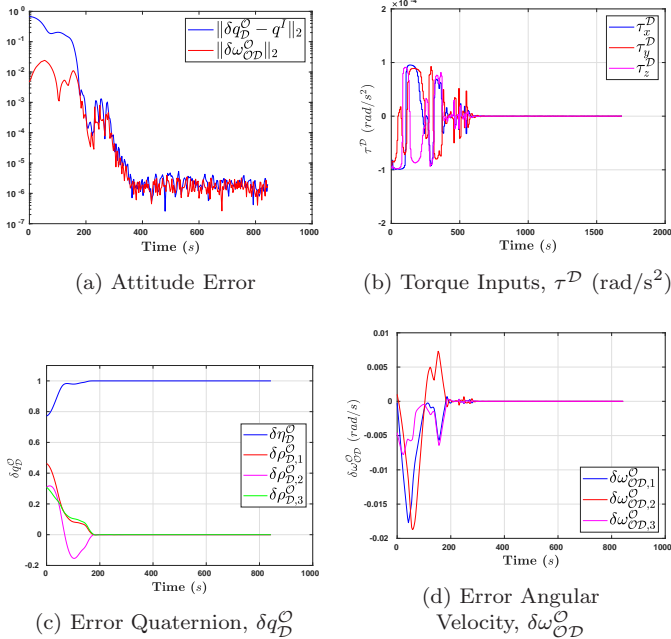


Fig. 8. Plots of the perturbed attitudinal error, states, and torque inputs for  $j_{max} = 3$ .

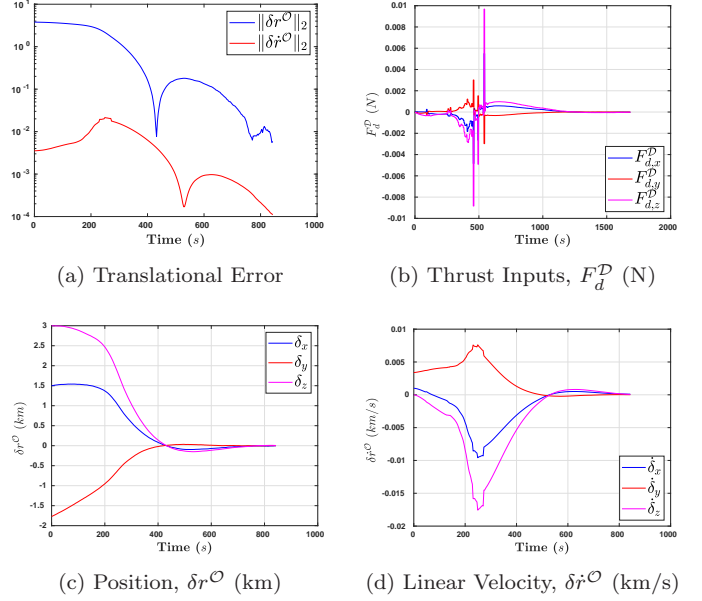


Fig. 9. Plots of the perturbed translational error, states, and thrust inputs when  $j_{max} = 3$ .

Table 3: Solver times and reductions for Problem 3 with perturbations

$j_{max}$	Average Time/Loop Reduction (s)	Average Time/Loop Reduction (%)	Maximum Loop Time Reduction (s)	Maximum Loop Time Reduction (%)
2	0.3616	36.16%	26.64	95.80%
3	0.2385	23.85%	26.33	94.70%
4	0.2029	20.29%	26.66	95.86%
5	0.2396	23.96%	26.65	95.86%

## 5. CONCLUSION

We proposed a time-constrained MPC control strategy for the 6 degree of freedom ARPOD problem, and showed that we can achieve the desired docking configuration under restrictive computational time constraints. Moreover, we demonstrated the robustness of docking using time-constrained MPC where the states of the system were subject to perturbations.

## REFERENCES

- (2022). Esa's annual space environment report. Technical Report GEN-DB-LOG-00288-OPS-SD, ESA Space Debris Office, Darmstadt, Germany.
- Bernhard, B., Choi, C., Rahmani, A., Chung, S.J., and Hadaegh, F. (2020). Coordinated motion planning for on-orbit satellite inspection using a swarm of small-spacecraft. In *2020 IEEE Aerospace Conference*, 1–13.
- Bourdarie, S. and Xapsos, M. (2008). The near-earth space radiation environment. *IEEE transactions on nuclear science*, 55(4), 1810–1832.
- Cheng, A.F., Rivkin, A.S., Michel, P., Atchison, J., Barnouin, O., Benner, L., Chabot, N.L., Ernst, C., Fahnestock, E.G., Kueppers, M., et al. (2018). Aida dart asteroid deflection test: Planetary defense and science objectives. *Planetary and Space Science*, 157, 104–115.
- Curtis, H. (2013). *Orbital mechanics for engineering students*. Butterworth-Heinemann.
- Di Cairano, S., Park, H., and Kolmanovsky, I. (2012). Model predictive control approach for guidance of space-

- craft rendezvous and proximity maneuvering. *Int. J. of Robust and Nonlinear Control*, 22(12), 1398–1427.
- Dong, H., Hu, Q., and Akella, M. (2018). Dual-quaternion-based spacecraft autonomous rendezvous and docking under six-degree-of-freedom motion constraints. *J. of Guidance, Control, and Dynamics*, 41(5), 1150–1162.
- Falcone, P., Tufo, M., Borrelli, F., Asgari, J., and Tseng, H.E. (2007). A linear time varying model predictive control approach to the integrated vehicle dynamics control problem in autonomous systems. In *2007 46th IEEE Conference on Decision and Control*, 2980–2985.
- Graichen, K. and K apernick, B. (2012). *A real-time gradient method for nonlinear model predictive control*. INTECH Open Access Publisher London.
- Graichen, K. and Kugi, A. (2010). Stability and incremental improvement of suboptimal mpc without terminal constraints. *IEEE Trans. on Automatic Control*, 55(11), 2576–2580.
- Gr une, L. and Pannek, J. (2017). Nonlinear model predictive control. In *Nonlinear model predictive control*, 45–69. Springer.
- Hartley, E.N. (2015). A tutorial on model predictive control for spacecraft rendezvous. In *2015 European Control Conference (ECC)*, 1355–1361. IEEE.
- Hartley, E.N. and Maciejowski, J.M. (2013). Graphical fpga design for a predictive controller with application to spacecraft rendezvous. In *52nd IEEE Conference on Decision and Control*, 1971–1976.
- Hogan, E.A. and Schaub, H. (2014). Attitude parameter inspired relative motion descriptions for relative orbital motion control. *Journal of Guidance, Control, and Dynamics*, 37(3), 741–749.
- Hu, Q., Yang, H., Dong, H., and Zhao, X. (2021). Learning-based 6-dof control for autonomous proximity operations under motion constraints. *IEEE Trans. on Aerospace and Electronic Systems*, 57(6), 4097–4109.
- Jewison, C.M. (2017). *Guidance and Control for Multi-Stage Rendezvous and Docking Operations in the Presence of Uncertainty*. Ph.D. thesis, Massachusetts Institute of Technology.
- Kuipers, J.B. (1999). *Quaternions and rotation sequences: a primer with applications to orbits, aerospace, and virtual reality*. Princeton university press.
- Lee, U. and Mesbahi, M. (2017). Constrained autonomous precision landing via dual quaternions and model predictive control. *Journal of Guidance, Control, and Dynamics*, 40(2), 292–308.
- Leomanni, M., Rogers, E., and Gabriel, S.B. (2014). Explicit model predictive control approach for low-thrust spacecraft proximity operations. *Journal of Guidance, Control, and Dynamics*, 37(6), 1780–1790.
- Li, Q., Yuan, J., Zhang, B., and Gao, C. (2017). Model predictive control for autonomous rendezvous and docking with a tumbling target. *Aerospace Science and Technology*, 69, 700–711.
- Lovelly, T.M. and George, A.D. (2017). Comparative analysis of present and future space-grade processors with device metrics. *Journal of Aerospace Information Systems*, 14(3), 184–197.
- Lovelly, T.M. (2017). *Comparative Analysis of Space-Grade Processors*. Ph.D. thesis, University of Florida.
- Malyuta, D., Yu, Y., Elango, P., and Aıkmee, B. (2021). Advances in trajectory optimization for space vehicle control. *Annual Reviews in Control*, 52, 282–315.
- Mayne, D.Q. (2014). Model predictive control: Recent developments and future promise. *Automatica*, 50(12), 2967–2986.
- Ogilvie, A., Allport, J., Hannah, M., and Lymer, J. (2008). Autonomous robotic operations for on-orbit satellite servicing. In *Sensors and Systems for Space Applications II*, volume 6958, 50–61.
- Pavlov, A., Shames, I., and Manzie, C. (2019). Early termination of nmpc interior point solvers: Relating the duality gap to stability. In *2019 18th European Control Conference (ECC)*, 805–810. IEEE.
- Petersen, C., Jaunzemis, A., Baldwin, M., Holzinger, M., and Kolmanovsky, I. (2014). Model predictive control and extended command governor for improving robustness of relative motion guidance and control. In *Proc. AAS/AIAA space flight mechanics meeting*.
- Richards, A. and How, J.P. (2003). Model predictive control of vehicle maneuvers with guaranteed completion time and robust feasibility. In *2003 American Control Conference*, volume 5, 4034–4040.
- Soderlund, A.A. and Phillips, S. (2022). Autonomous rendezvous and proximity operations of an underactuated spacecraft via switching controls. In *AIAA SCITECH 2022 Forum*, 0956.
- Soderlund, A.A., Phillips, S., Zaman, A., and Petersen, C.D. (2021). Autonomous satellite rendezvous and proximity operations via geometric control methods. In *AIAA Scitech 2021 Forum*, 0075.
- Sun, L. and Huo, W. (2015). 6-dof integrated adaptive backstepping control for spacecraft proximity operations. *IEEE Transactions on Aerospace and Electronic Systems*, 51(3), 2433–2443.
- Trivailo, P.M., Wang, F., and Zhang, H. (2009). Optimal attitude control of an accompanying satellite rotating around the space station. *Acta Astronautica*, 64(2-3), 89–94.
- W achter, A. and Biegler, L.T. (2006). On the implementation of an interior-point filter line-search algorithm for large-scale nonlinear programming. *Mathematical programming*, 106(1), 25–57.
- Wang, X., Wang, Z., and Zhang, Y. (2018). Model predictive control to autonomously approach a failed spacecraft. *Int. J. of Aerospace Engineering*, 2018.
- Wang, Y. and Ji, H. (2019). Integrated relative position and attitude control for spacecraft rendezvous with iss and finite-time convergence. *Aerospace Science and Technology*, 85, 234–245.
- Yang, J. and Stoll, E. (2019). Adaptive sliding mode control for spacecraft proximity operations based on dual quaternions. *Journal of Guidance, Control, and Dynamics*, 42(11), 2356–2368.
- Zhou, B.Z., Liu, X.F., and Cai, G.P. (2020). Motion-planning and pose-tracking based rendezvous and docking with a tumbling target. *Advances in Space Research*, 65(4), 1139–1157.